<u>Supporting Information</u>

The aerosol-assisted chemical vapour deposition of Mo-doped BiVO$_4$ photoanodes for solar water splitting: an experimental and computational study

Shaobin Zhao,[a] Chenglin Jia,[b] Xinyi Shen,[a] Ruohao Li,[a] Louise Oldham,[a] Benjamin Moss,[a] Brian Tam,[c] Sebastian Pike,[d] Nicholas Harrison,[a,e] Ehsan Ahmad[a,e]* and Andreas Kafizas[a,f]*

[a]*Department of Chemistry, Molecular Science Research Hub, Imperial College London, White City, London, W12 0BZ, U.K.*

[b]*Department of Chemistry, University College London, 20 Gordon Street, London, WC1H 0AJ, U.K.*

[c]*Department of Physics, Imperial College London, South Kensington, London, SW7 2AZ, U.K.*

[d]*Department of Chemistry, University of Warwick, Coventry, CV4 7AL, U.K.*

[e]*Thomas Young Centre, The London Centre for the Theory and Simulation of Materials, Royal School of Mines, Imperial College London, South Kensington, London, U.K.*

[f]*London Centre for Nanotechnology, Imperial College London, South Kensington, London, SW7 2AZ, U.K.*

*co-corresponding authors: a.kafizas@imperial.ac.uk and ehsan.ahmad08@imperial.ac.uk

1. Synthesis & Precursor Speciation
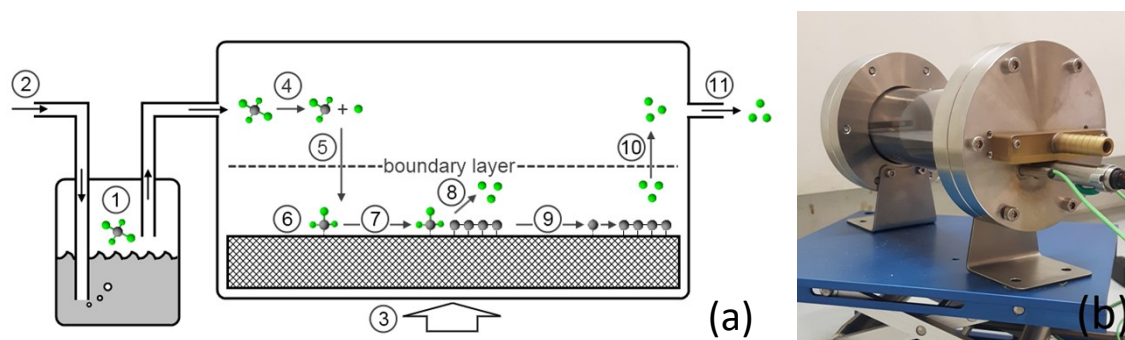
Figure S1: (a) A schematic covering the key stages common to all chemical vapour deposition (CVD) processes for thin film growth: (1) vapour generation (heat, sonication, atomisation etc), (2) transport (inert carrier gas), (3) activation (heat, plasma, light, etc), (4) gas phase reactions, (5) reactant diffusion, (6) absorption, (7) growth site diffusion, (8) surface reactions, (9) nucleation, (10) by-product diffusion, (11) by-products to exhaust. (b) A photograph of the aerosol-assisted chemical vapour deposition (AA-CVD) apparatus used to grow our BiVO$_4$ and Mo-doped BiVO$_4$ photoanodes on FTO glass.
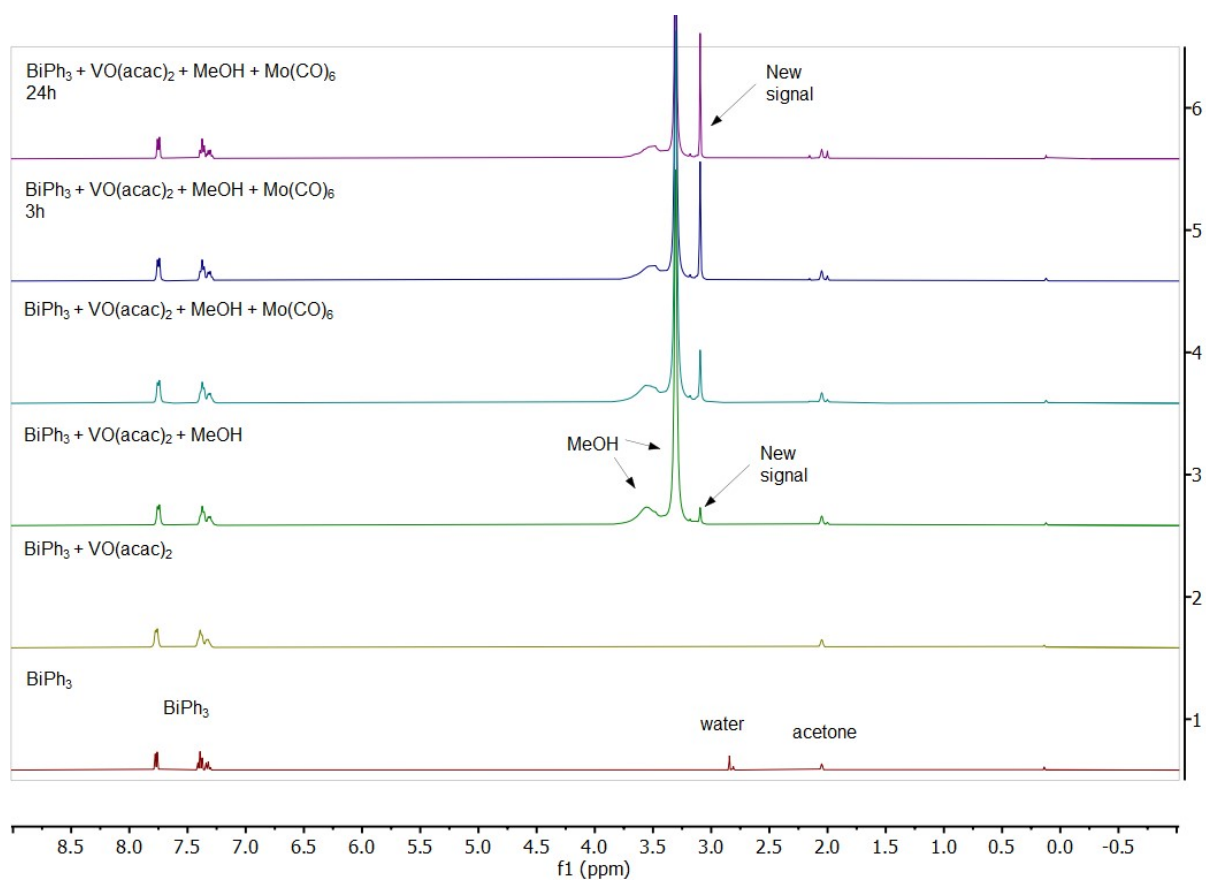
Figure S2a: ^{1}H NMR spectra of precursor mixture in d^6-acetone (0.5 mL + 50 μL MeOH; 85 mM VO(acac)$_2$ and BiPh$_3$, <8mM Mo(CO)$_6$ (partially dissolved)). Signals for BiPh$_3$ remain unchanged, the 'new signal' may be attributed to new OMe signals coordinated to V(V) such as [VO(OMe)(acac)$_2$] [VO(OMe)$_3$] and [VO(OMe)$_2$(acac)]$_2$. Small free acac-H signals are also located at 5.6 & 2.0 ppm.
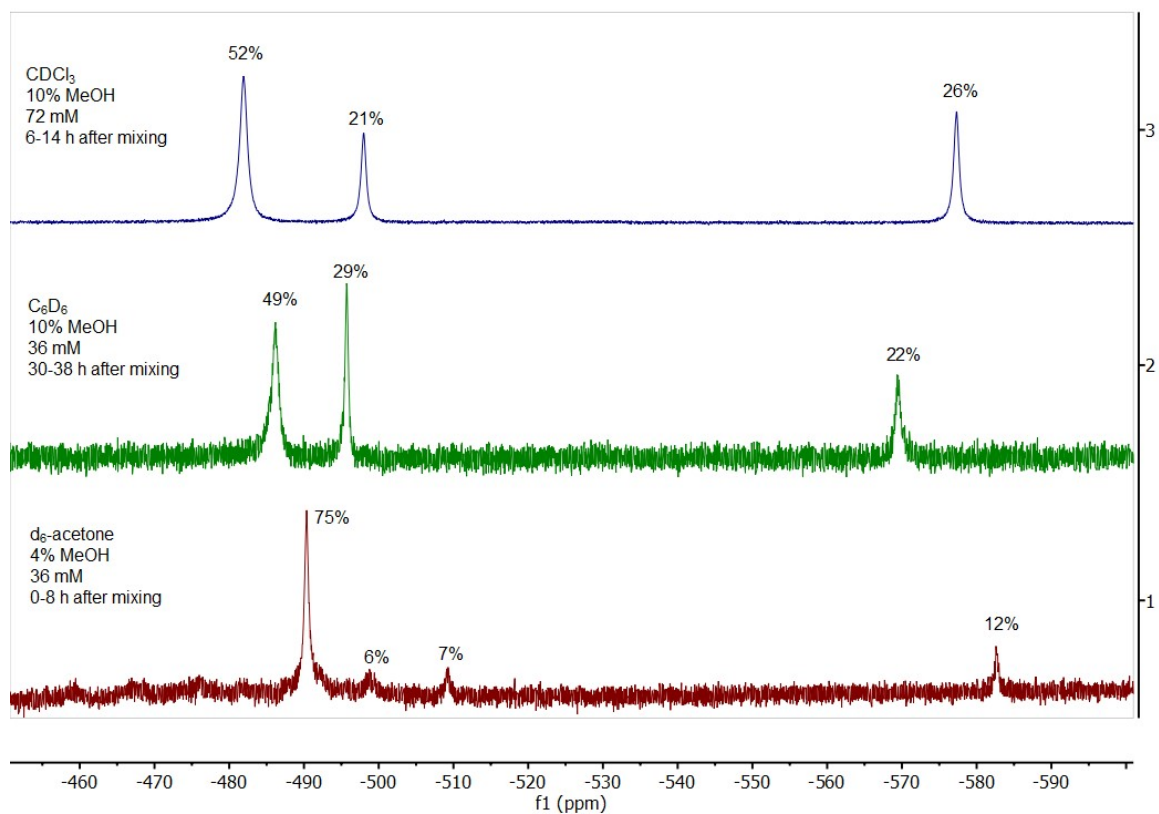
Figure S2b: ^{51}V NMR spectra of VO(acac)$_2$ + MeOH dissolved in various solvents after ageing under air.
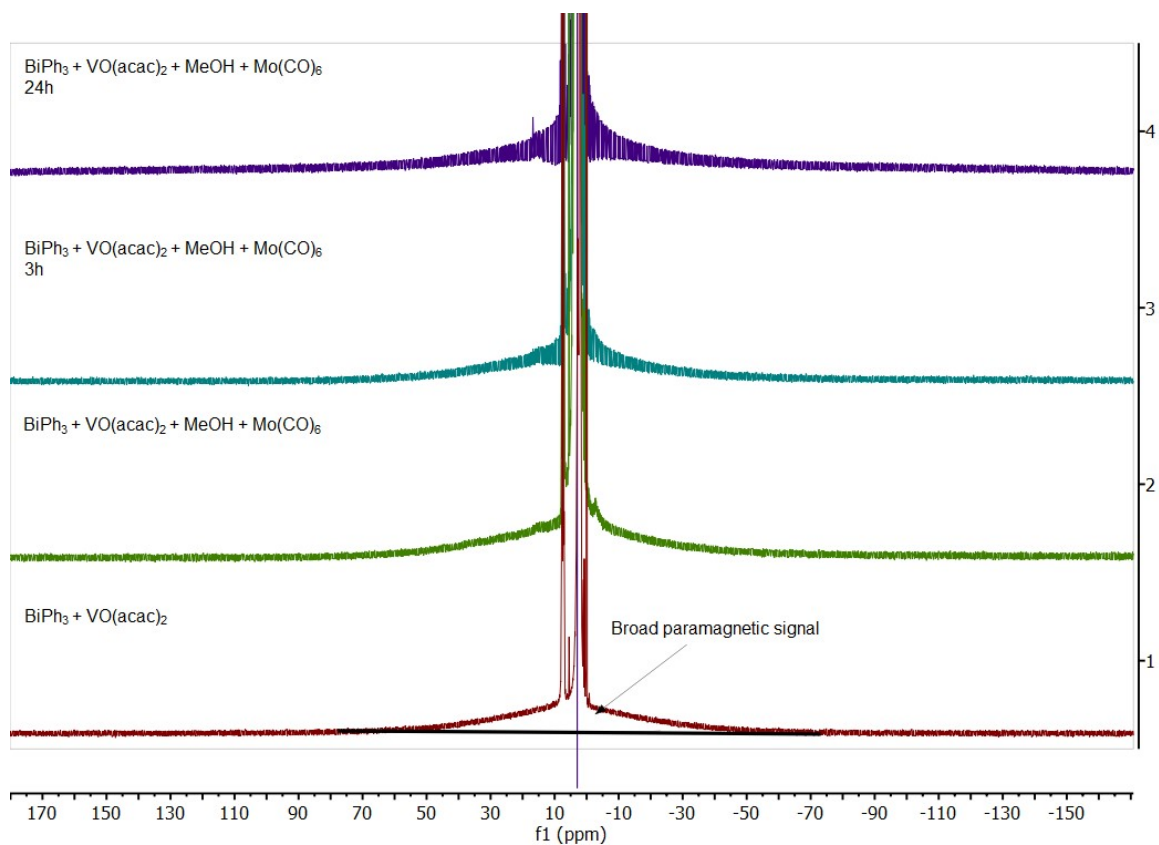
Figure S2c: ^1H NMR spectra of precursor mixture in d^6-acetone, showing broad paramagnetic signal associated with V(IV) species, which diminishes over ageing time.
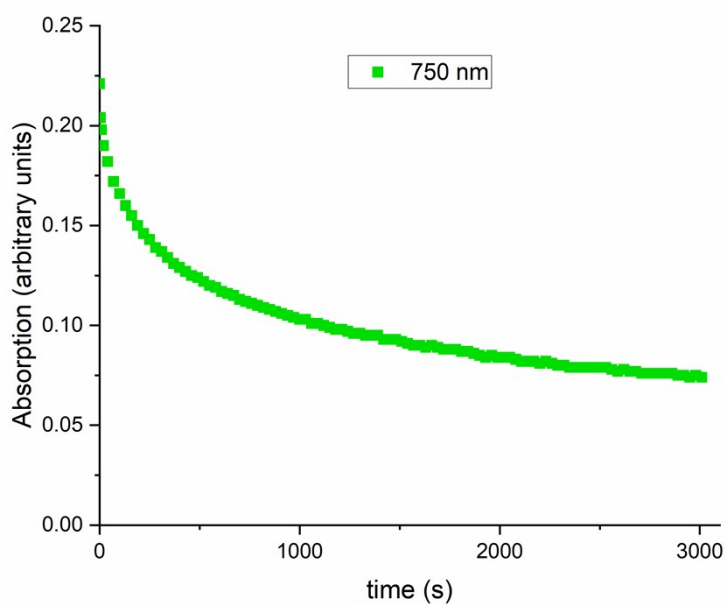

Figure S2d: Visible absorption of a 5mM solution of $VO(acac)_2$ in acetone/MeOH (3:1) under air over time at 750 nm. This signal corresponds to the d-d transition in V(IV) complexes. The cuvette was sealed with 2 mL solution and ~2 mL headspace.
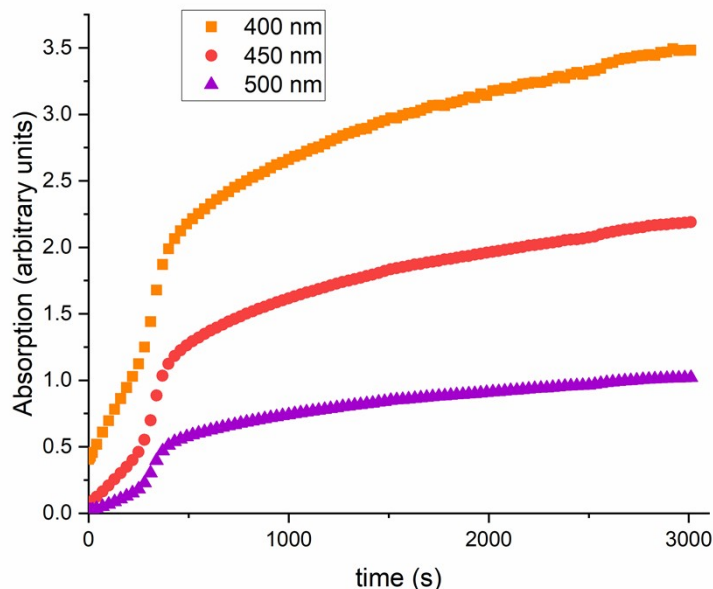
Figure S2e: Visible absorption of a 5mM solution of VO(acac)$_2$ in acetone/MeOH (3:1) under air over time at 450, 500 and 550 nm. This absorption region is mainly caused by ligand to metal charge transfer in V(V) compounds. The cuvette was sealed with 2 mL solution and ~2 mL headspace.

2. Characterisation

(a)

(b)
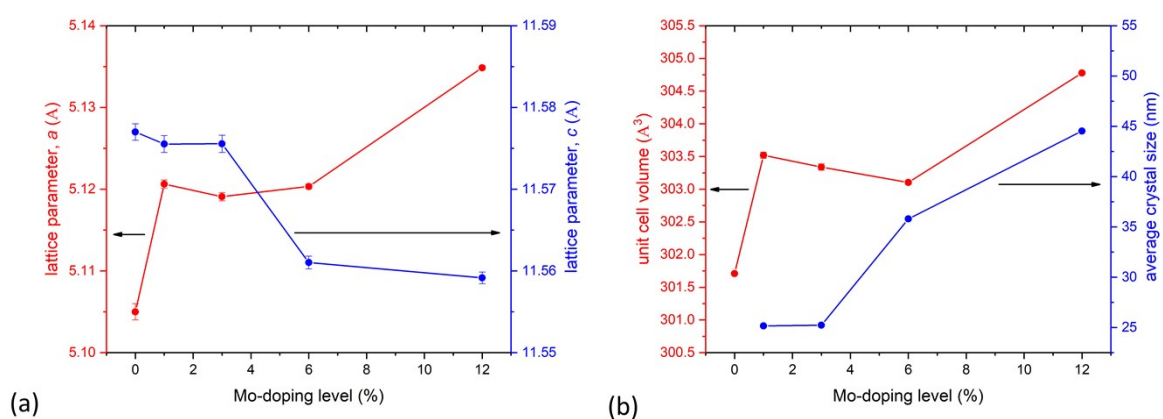
Figure S3: XRD derived (a) lattice parameters a and c (Å), and (b) unit cell volume (Å^3) and average crystal sizes (nm) as a function of Mo precursor doping level (%) in Mo-doped BiVO$_4$ (all values at 0% Mo-doping were taken from an undoped BiVO$_4$ standard.
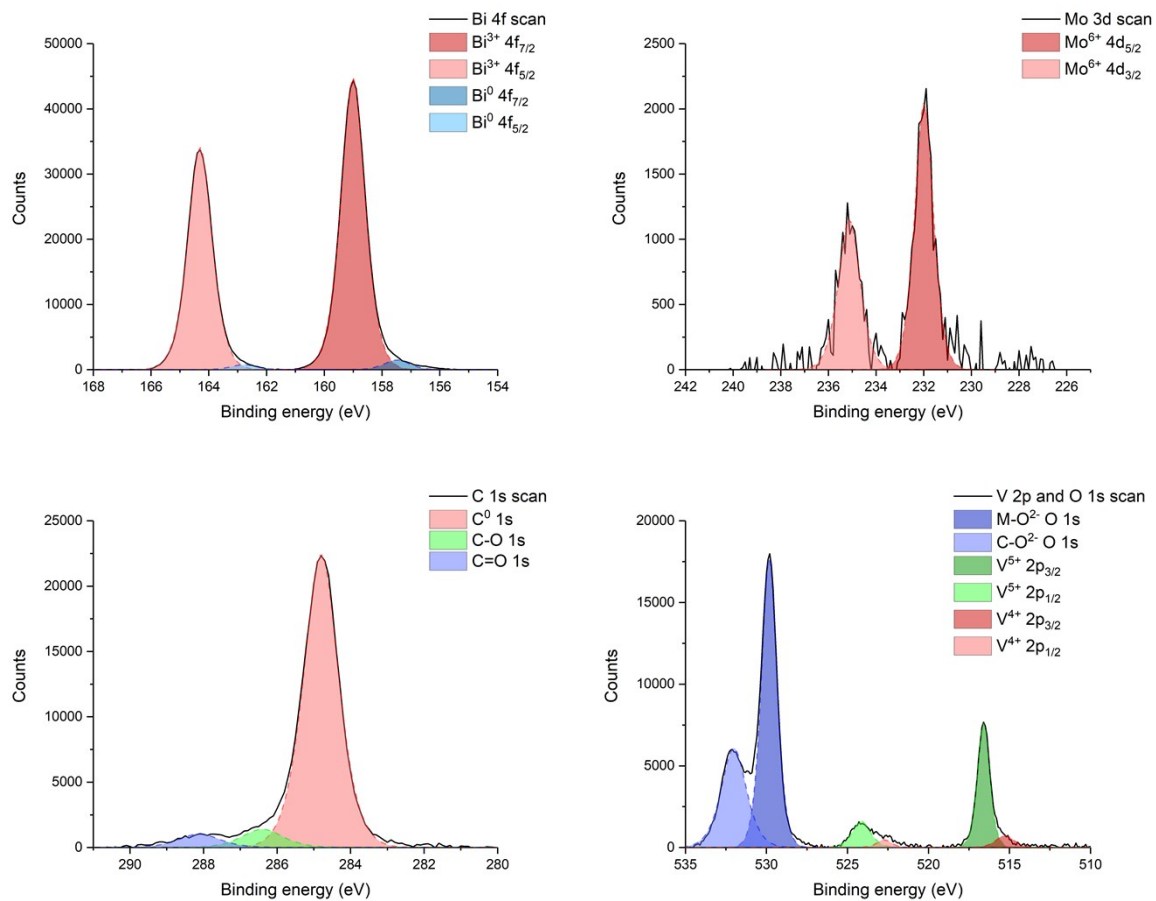
Figure S4: XPS analysis of a representative sample, 3%Mo-BiVO$_4$, showing the binding energy regions and contribution of each environment for Bi 4f, Mo 4d, C 1s and V 2p and O 1s.

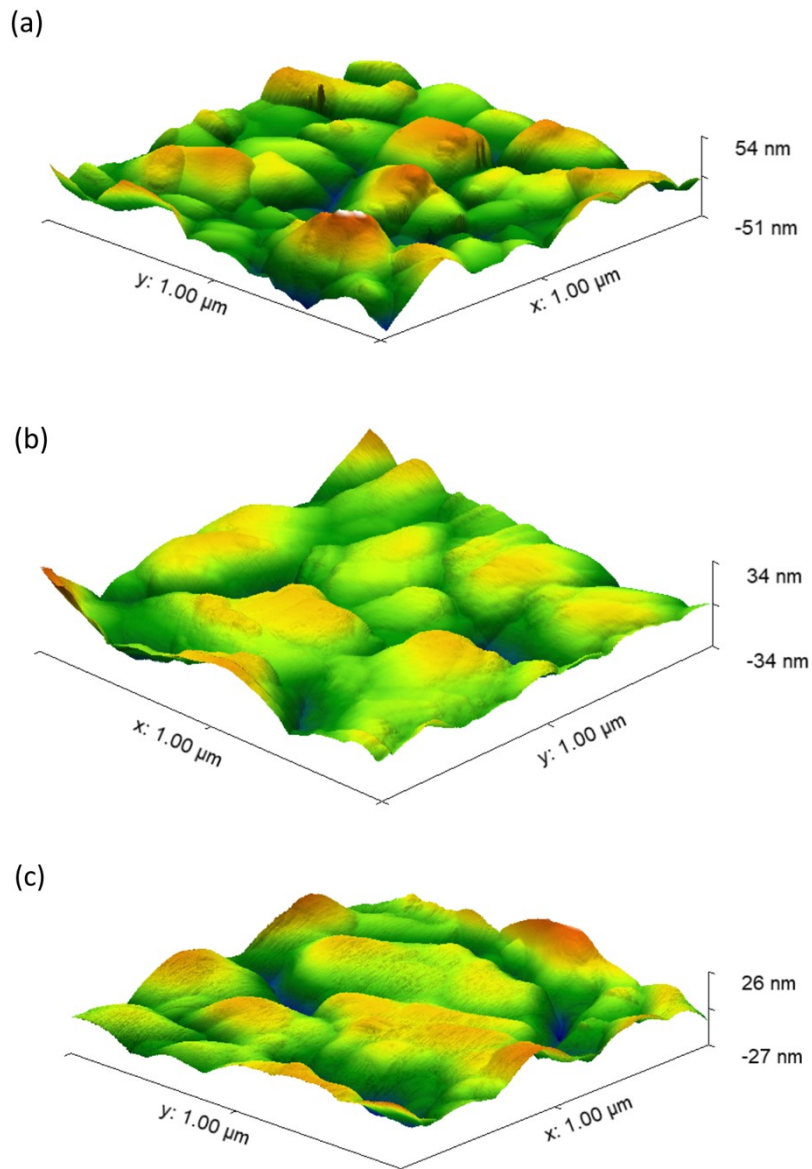|		BiVO$_4$	1%Mo-BiVO$_4$	3%Mo-BiVO$_4$	6%Mo-BiVO$_4$	12%Mo-BiVO$_4$
Binding energy (eV)	Bi^{3+} (4f$_{7/2}$)	158.6(2)	159.3(1)	158.6(1)	159.5(1)	159.4(2)
	Bi^0 (4f$_{7/2}$)	163.1(6)	162.7(1)	162.0(1)	162.9(1)	162.8(2)
	V^{5+} (2p$_{3/2}$)	516.1(2)	516.8(1)	516.1(1)	517.1(1)	516.9(2)
	V^{4+} (2p$_{3/2}$)	514.7(2)	515.4(1)	514.8(1)	515.7(1)	515.6(2)
	Mo^{6+} (3d$_{5/2}$)	-	232.4(1)	231.8(1)	232.6(1)	232.4(2)
	O^{2-} (1s)	529.3(2)	530.0(1)	529.3(1)	530.2(1)	530.0(2)
Abundance (%)	Bi^{3+}	4.9(1)	12.5(1)	7.0(8)	11.1(13)	13.6(4)
	Bi^0	-	0.1(1)	0.0(1)	0.1(1)	0.1(1)
	V^{5+}	2.6(1)	8.3(4)	4.0(6)	6.4(8)	8.0(4)
	V^{4+}	0.1(1)	0.4(1)	0.2(1)	0.4(1)	0.7(1)
	Mo^{6+}	-	0.2(1)	0.3(1)	1.0(1)	1.7(4)
	O^{2-}	15.1(1)	40.6(8)	23.1(32)	33.7(25)	37.4(5)
Mo: V (%)		0	2.0(1)	4.3(4)	9.6(4)	12.7(14)
VB edge (eV)		1.9(2)	1.9(1)	2.0(1)	1.9(1)	2.0(1)

Table S1: A summary of the modelled XPS data for the undoped BiVO$_4$ and series of Mo-doped BiVO$_4$ coatings. Each value represents the average of three measurements at difference locations across the sample. Numbers in brackets represent the standard error on the lowest significant figures.
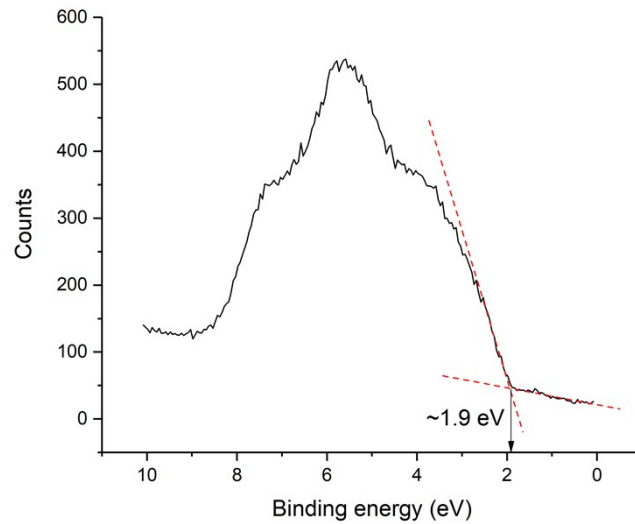
Figure S5: XPS measurement of the valence band energy environment in an undoped BiVO$_4$ coating. All energies were adjusted using the difference in the metal-oxygen core line in the O 1s environment (529.6 eV) to a reference value (529.8 eV). Extrapolation of the valence band maximum (VBM) revealed an energy of ~1.9 eV with respect to the Fermi level of the material.
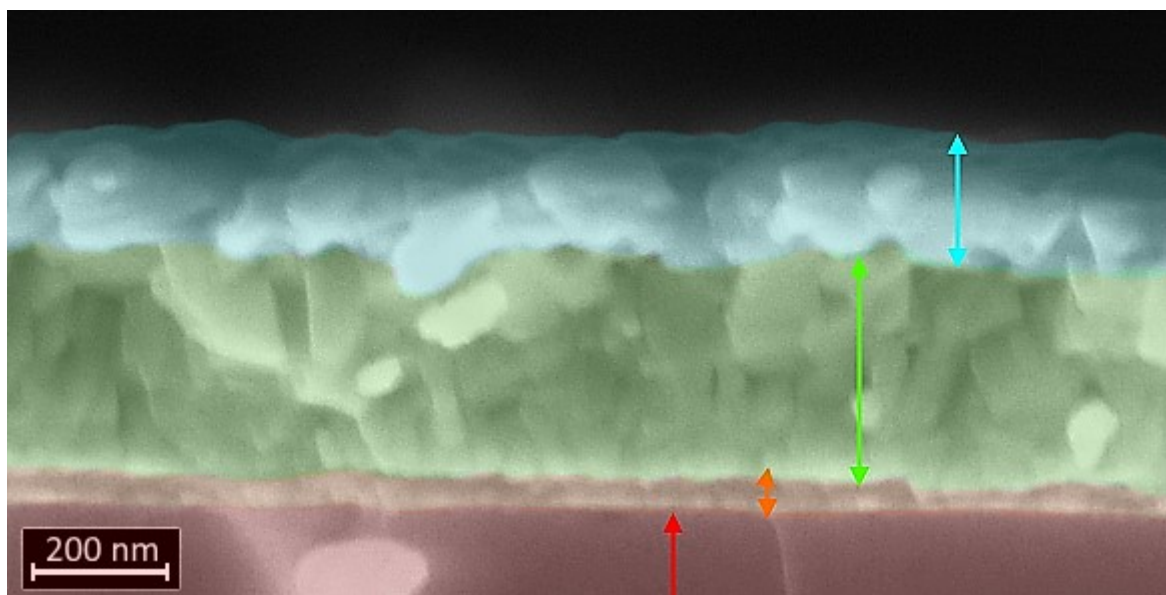
Figure S6: Side-on SEM image, taken at 100k magnification, of a representative sample (6%Mo-BiVO$_4$), where the red, orange, green and blue arrow bars show the relative thicknesses of the glass substrate (~3 mm thick), SiO$_2$ barrier layer (~35 nm thick), FTO layer (~320 nm thick) and BiVO$_4$ layer (~180 nm thick) respectively [the width of the image represents a distance of 1.5 µm].
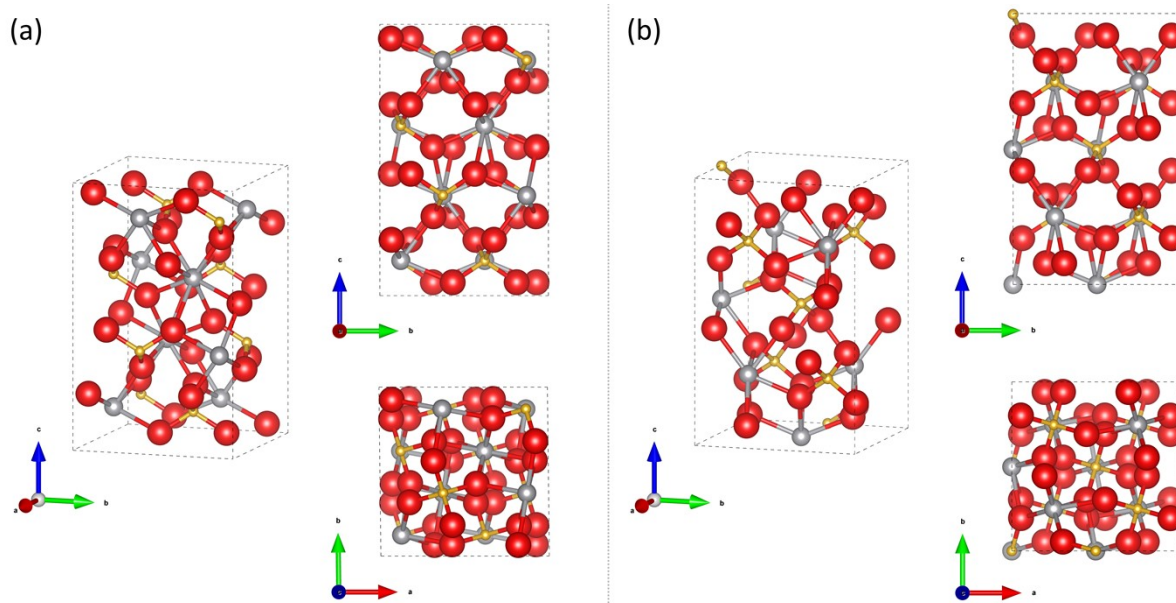
(a)

(b)

(c)

Figure S7: AFM images of (a) 1%Mo-BiVO$_4$, (b) 3%Mo-BiVO$_4$ and (c) 12%Mo-BiVO$_4$ samples, measured over a 1 µm x 1 µm square area.
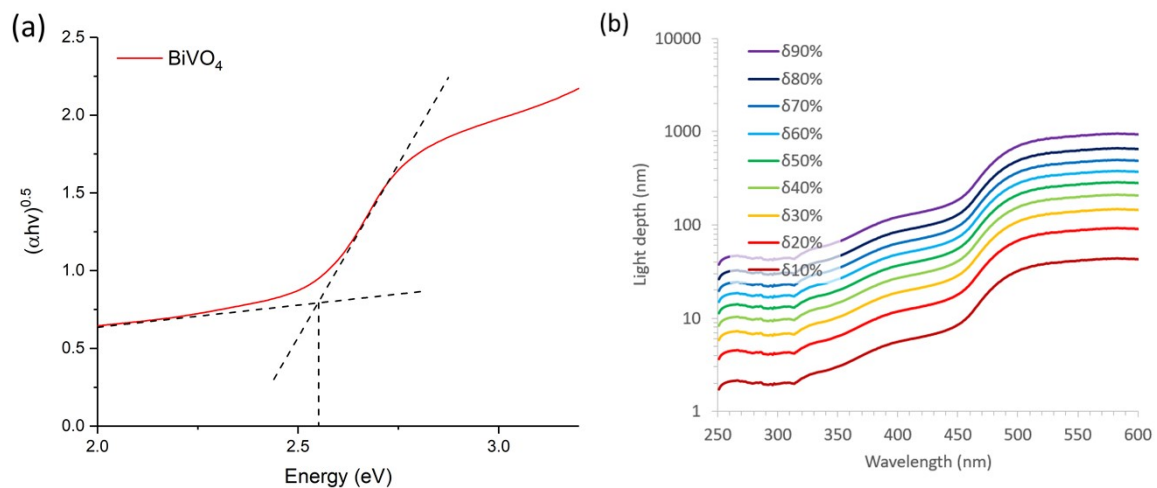
Figure S8: (a) Tauc plot of a representative undoped BiVO$_4$ sample showing the determination of the indirect allowed optical bandgap transition. (b) The light penetration depth (nm) for a range of transmission (10 to 90%) in the undoped BiVO$_4$ sample.


Figure S9: Calculated undoped structures of BiVO$_4$ showing angled, a axis and c axis views for (a) monoclinic clinobisvanite (m-BiVO$_4$) and (b) tetragonal scheelite (t-BiVO$_4$).
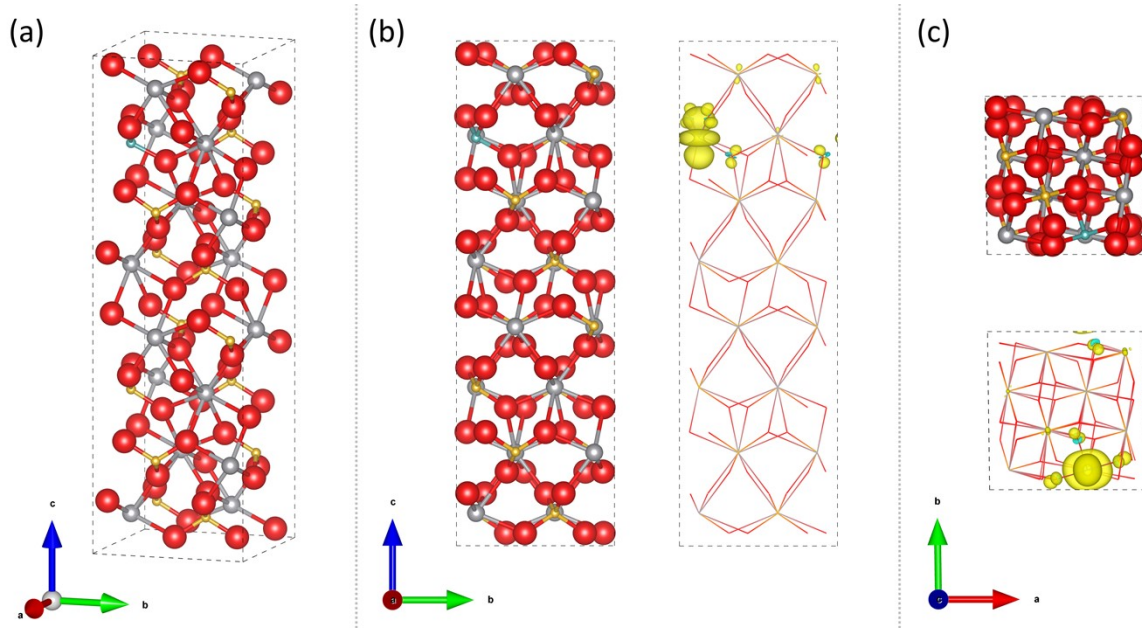
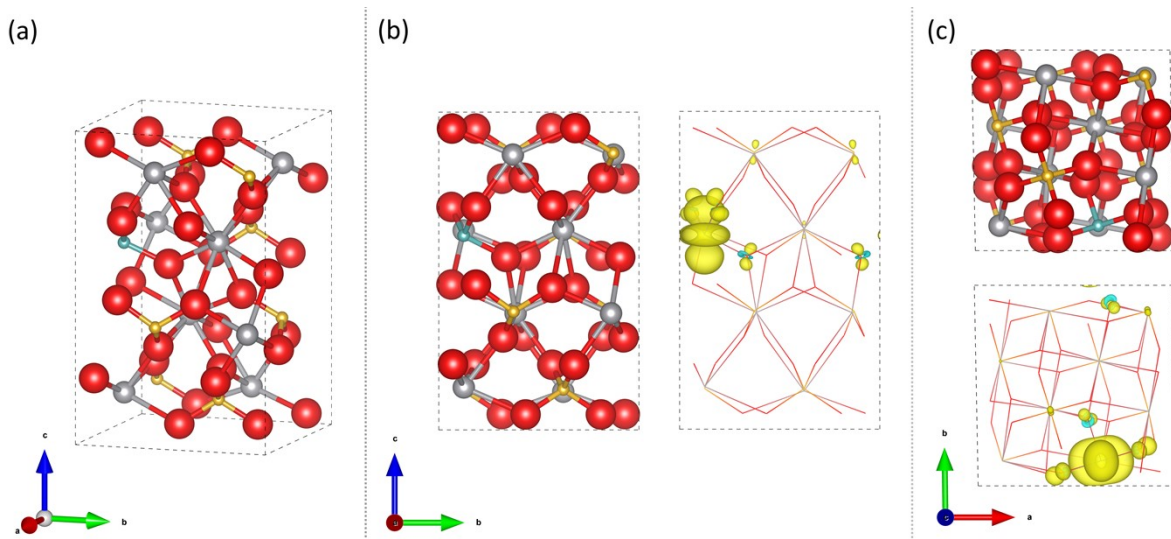**Figure S10**: Calculated structure for 6.25 at.% Mo doping of a V site in monoclinic clinobisvanite BiVO$_4$ for a 2 x 1 x 1 supercell showing atomic positions and spin density [Bi = silver, V = gold, O = red, Mo = light blue; ionic radii proportions scaled down for visibility]. (a) angled view, (b) a-axis view and (c) c-axis view.
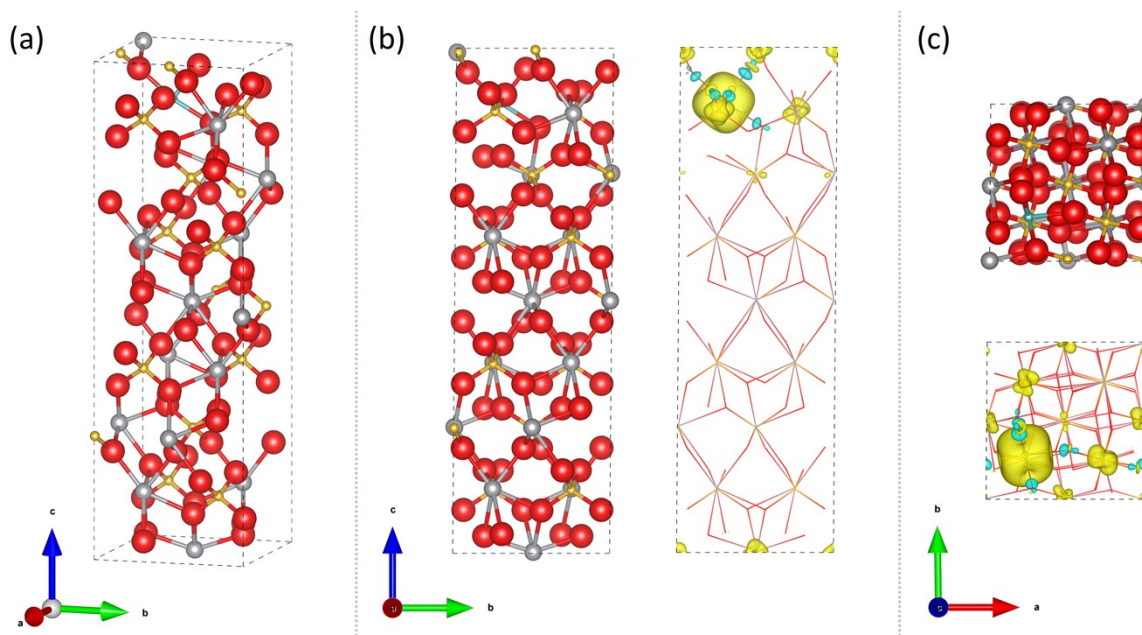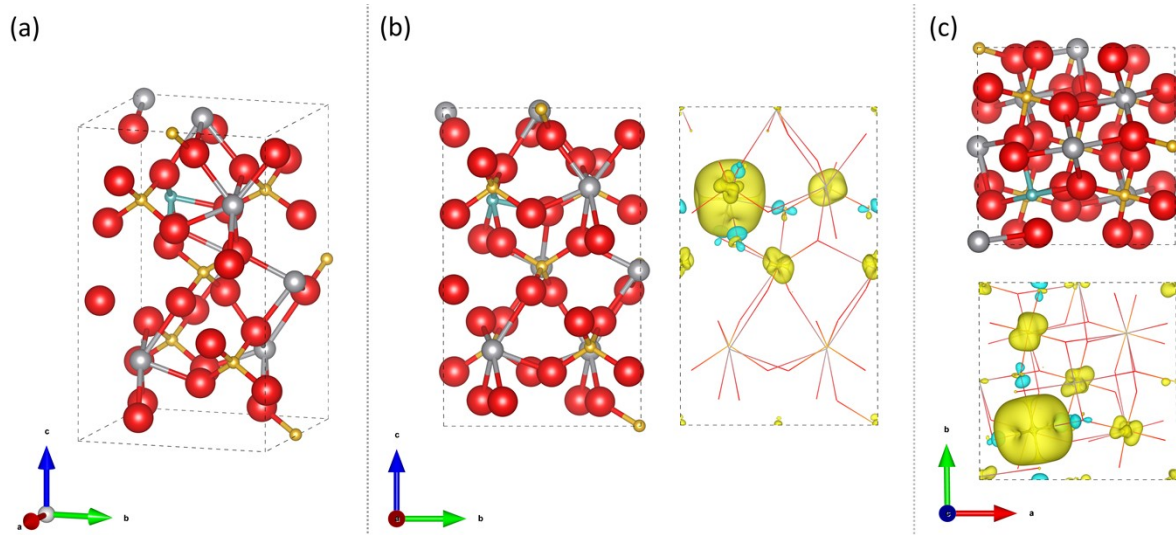

Figure S11: Calculated structure for 6.25 at.% Mo doping of a Bi site in tetragonal scheelite BiVO$_4$ for a 2 x 1 x 1 supercell showing atomic positions and spin density [Bi = silver, V = gold, O = red, Mo = light blue; ionic radii proportions scaled down for visibility]. (a) angled view, (b) a-axis view and (c) c-axis view.
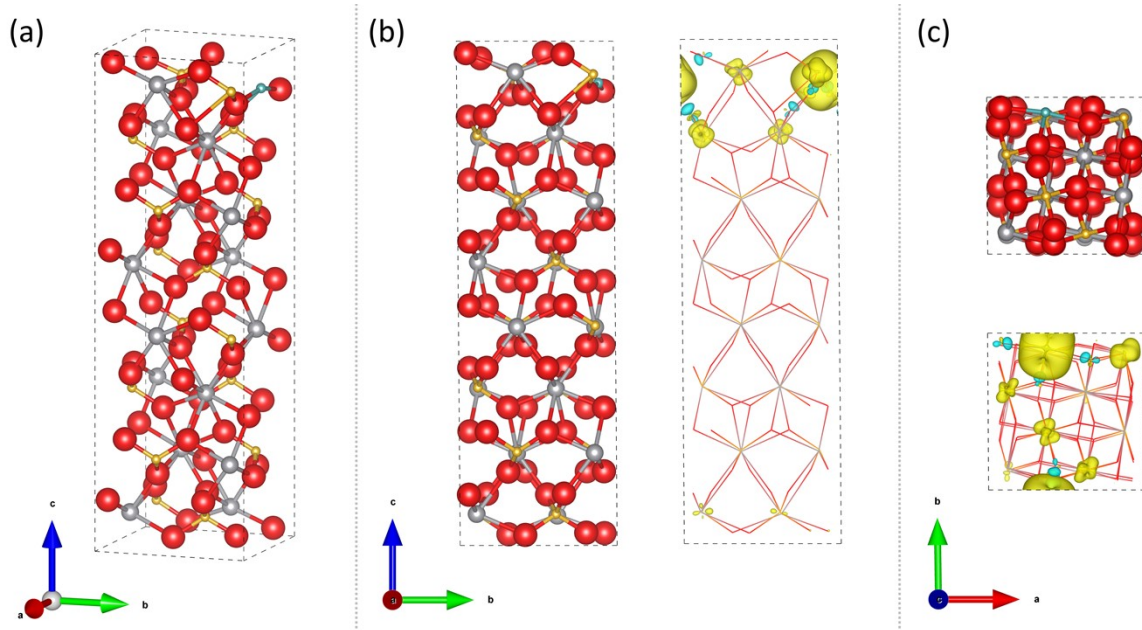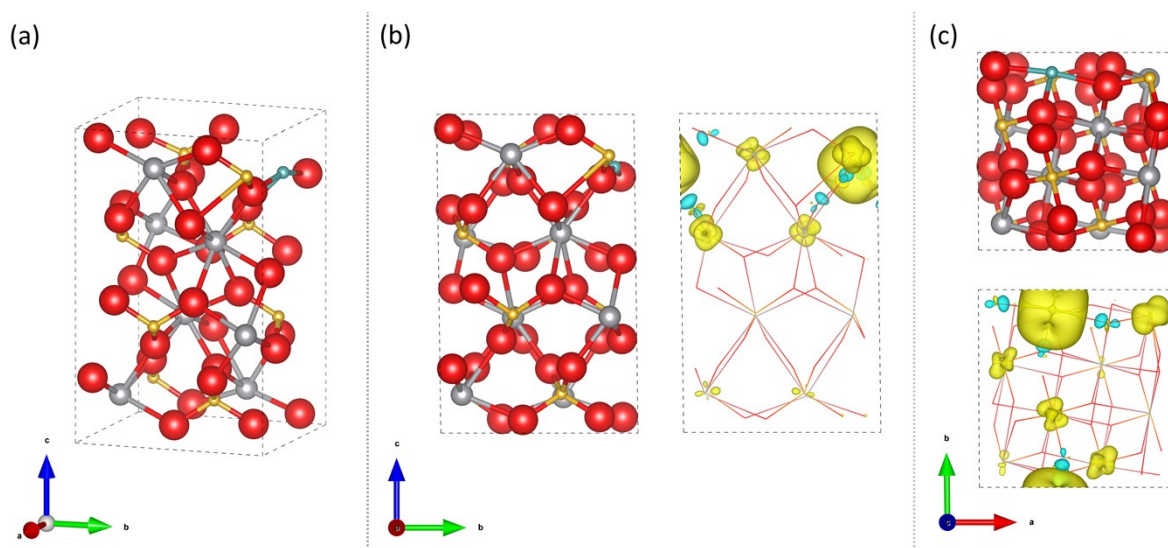
Figure S12: Calculated structure for 6.25 at.% Mo doping of a Bi site in monoclinic clinobisvanite $BiVO_4$ for a 2 x 1 x 1 supercell showing atomic positions and spin density [Bi = silver, V = gold, O = red, Mo = light blue; ionic radii proportions scaled down for visibility]. (a) angled view, (b) a-axis view and (c) c-axis view.


Figure S13: Calculated structure for 12.5 at.% Mo doping of a V site in monoclinic clinobisvanite $BiVO_4$ for a single unit cell showing atomic positions and spin density [Bi = silver, V = gold, O = red, Mo = light blue; ionic radii proportions scaled down for visibility]. (a) angled view, (b) a-axis view and (c) c-axis view.

Figure S14: Calculated structure for 12.5 at.% Mo doping of a Bi site in tetragonal scheelite BiVO$_4$ for a single unit cell showing atomic positions and spin density [Bi = silver, V = gold, O = red, Mo = light blue; ionic radii proportions scaled down for visibility]. (a) angled view, (b) a-axis view and (c) c-axis view.


Figure S15: Calculated structure for 12.5 at.% Mo doping of a Bi site in monoclinic clinobisvanite BiVO$_4$ for a single unit cell showing atomic positions and spin density [Bi = silver, V = gold, O = red, Mo = light blue; ionic radii proportions scaled down for visibility]. (a) angled view, (b) a-axis view and (c) c-axis view.
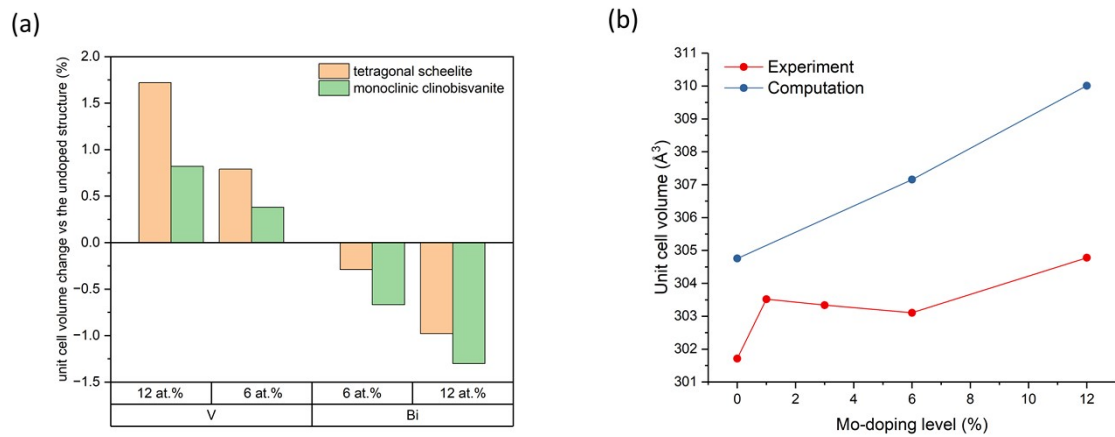
Figure S16: (a) Comparison of the calculated percentage changes in unit cell volume for the tetragonal and monoclinic forms of $BiVO_4$ upon doping for 6.25 and 12.5 at.% Mo-doping replacing a V or Bi site. (b) Comparison of the changes in unit cell volume for calculations and experiment for t-$BiVO_4$.
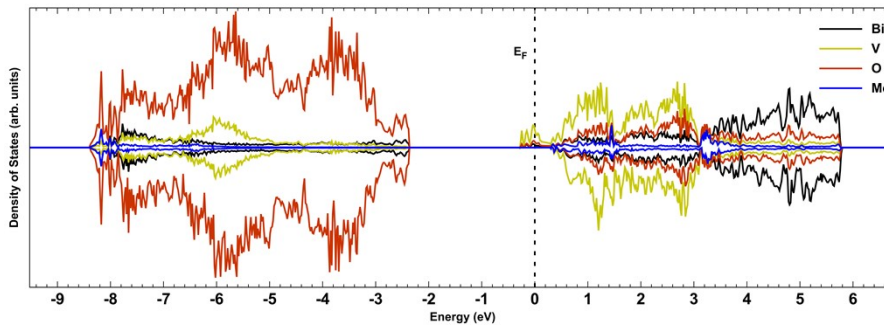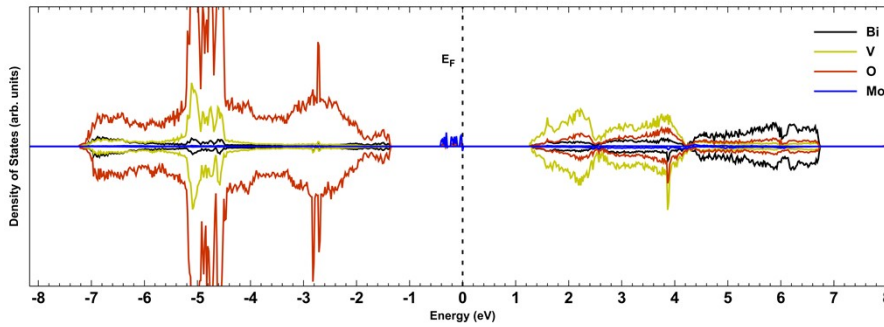
undoped
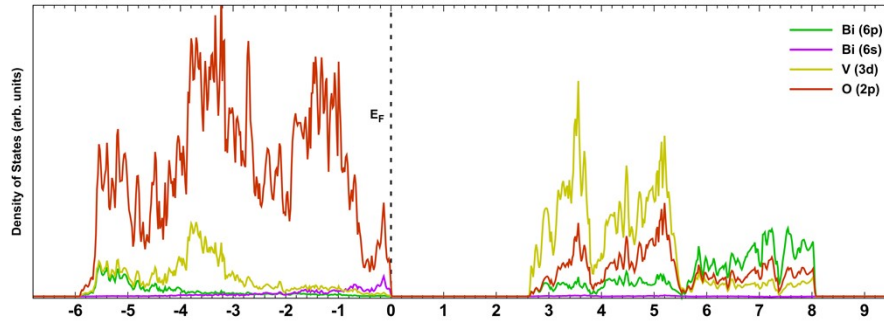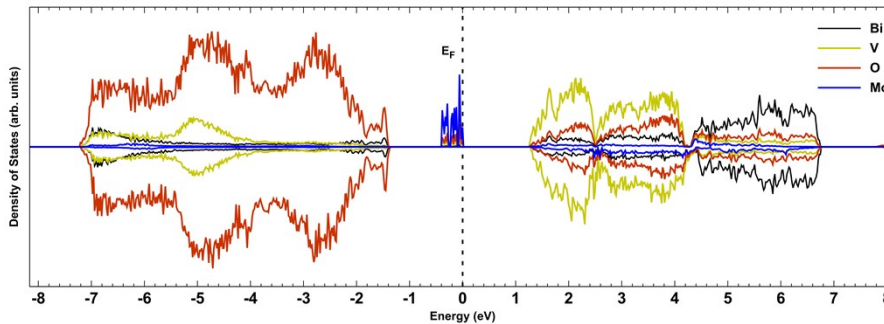

6.25 at.% Mo in a V site
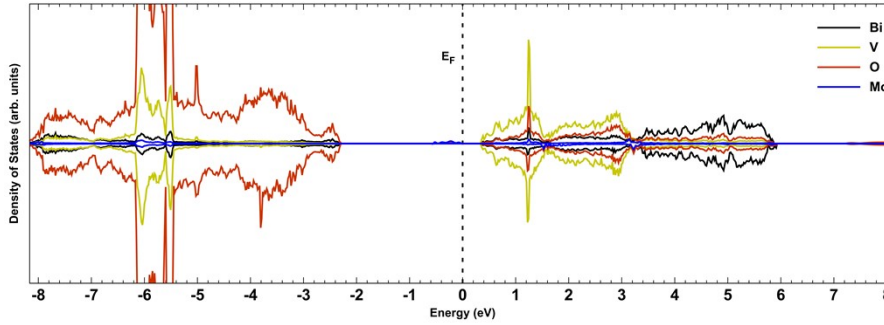
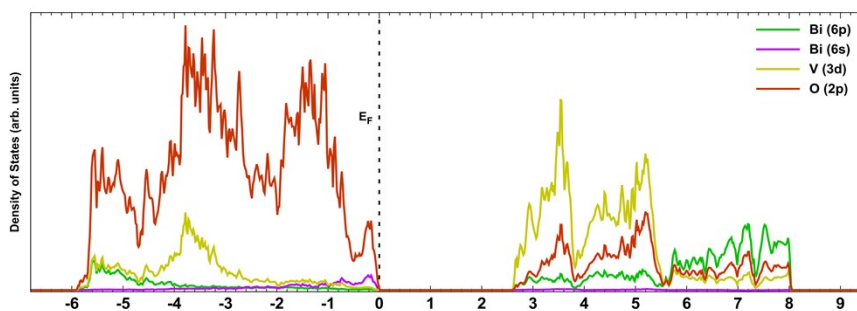## 12.5 at.% Mo in a V site

6.25 at.% Mo in a Bi site

12.5 at.% Mo in a Bi site
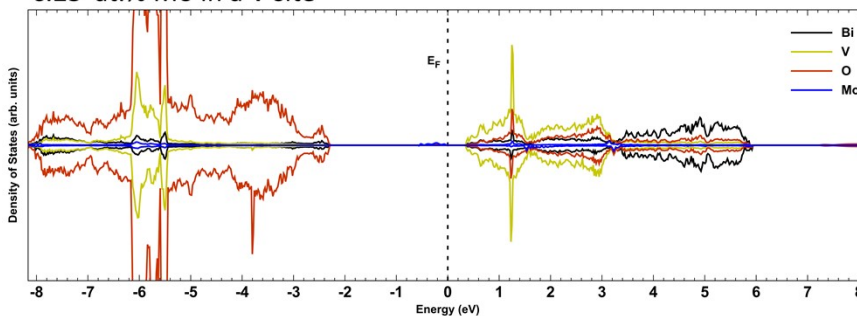
Figure S17: Full scale PDOS of all calculate tetragonal scheelite BiVO$_4$ structures herein, including undoped, 6.25 at.% Mo replacing a V site, 12.5 at.% Mo replacing a V site, 6.25 at.% Mo replacing a Bi site, and a 12.5 at.% Mo replacing a Bi site. For the undoped samples, the individual orbital contributions to the PDOS are shown.
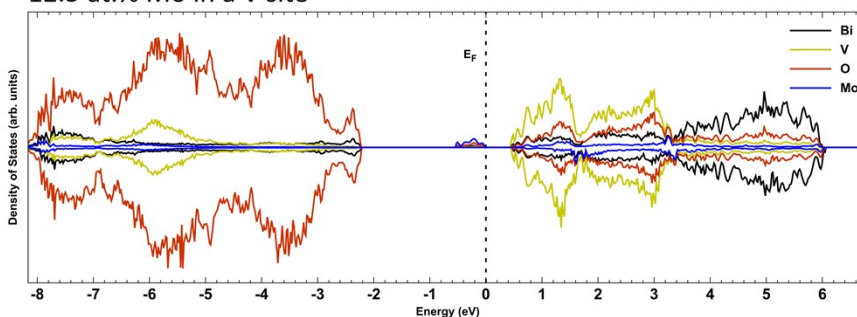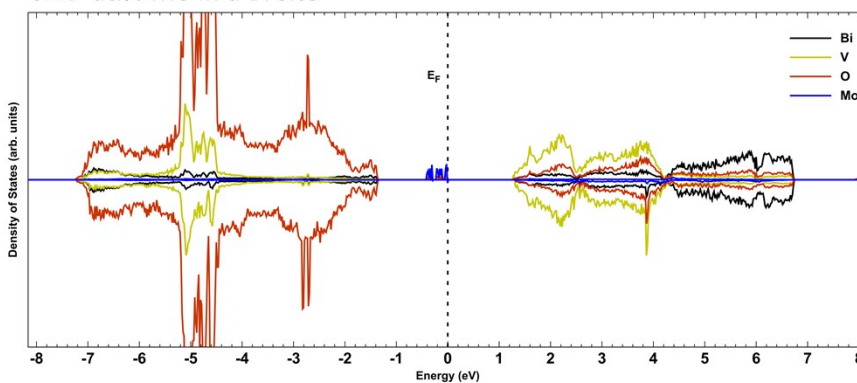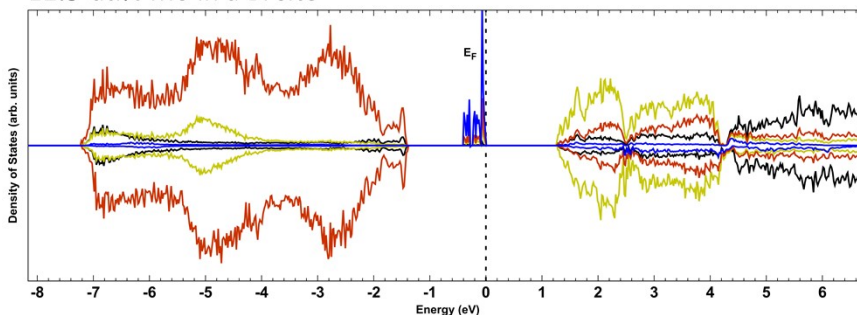
undoped

6.25 at.% Mo in a V site


12.5 at.% Mo in a V site

6.25 at.% Mo in a Bi site

12.5 at.% Mo in a Bi site

Figure S18: Full scale PDOS of all calculate monoclinic clinobisvanite $BiVO_4$ structures herein, including undoped, 6.25 at.% Mo replacing a V site, 12.5 at.% Mo replacing a V site, 6.25 at.% Mo replacing a Bi site, and a 12 .5 at.% Mo replacing a Bi site. For the undoped samples, the individual orbital contributions to the PDOS are shown.
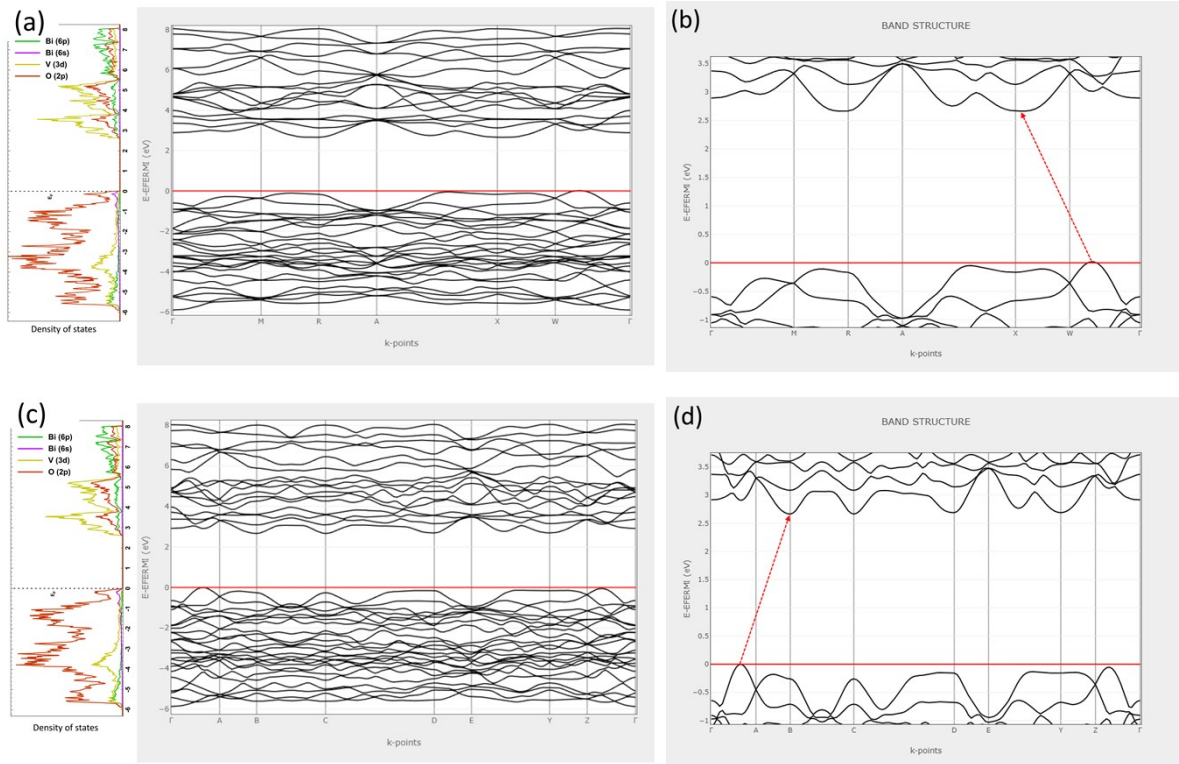
Figure S19: Electronic structures of (a, b) t-$BiVO_4$ and (c, d) m-$BiVO_4$. Figures (a) and (c) show the projected density of states and the individual atomic orbital contributions alongside the electronic structures. Figures (b) and (d) show a close up of the bandgap region in the electronic structures, as well as the lowest energy transition from the valence band maximum to the conduction band minimum, with each case being indirect.